Tuning bandgap and optical properties of Pb-free perovskites $RbGeX_3$ (X = Cl, Br and I) under pressure: a DFT study

[1] Bewar M. Ahmad, [2] Nawzad A. Abdulkareem and [3] Sarkawt A. Sami

[1] Department of Physics, Faculty of Science, University of Zakho, Kurdistan Region, Iraq bewar.mohammed@uoz.edu.krd
[2] Department of Physics, Faculty of Science, University of Zakho, Kurdistan Region, Iraq nawzad.abdulkareem@uoz.edu.krd
[3] Department of Physics, College of Science, University of Duhok, Kurdistan Region, Iraq sarkawt@uod.ac

Received: 11.05.2023

Abstract. We study structural, electronic and optical properties of inorganic lead-free halide perovskites $RbGeX_3$ (X = Cl, Br and I) under hydrostatic pressure, which could facilitate development of new optoelectronic and solar-cell technologies. *ab initio* first-principles calculations are employed based on the generalized gradient approximation within the framework of density functional theory. We demonstrate that the bandgap of our perovskites decreases with increasing pressure. At a given pressure, the bandgap becomes narrower when the halogen atom is changed from Cl to I. We also examine the density of states and demonstrate that the energy levels near the Fermi level change significantly under pressure. The optical properties are calculated using the density functional perturbation theory and the Kramers–Kronig relation. The optical parameters such as the real and imaginary parts of the dielectric function, the refractive index and the absorption coefficient are calculated under different pressures.

Keywords: electronic band structure, bandgap energy, density of states, optical properties, hydrostatic pressure, density functional theory, generalized gradient approximation

UDC: 535.3

1. Introduction

Perovskite materials have recently emerged as a promising solution in energy conversion, particularly in the field of solar cells [1]. These materials reveal excellent photoelectric properties [2]. They have been found to be highly efficient in converting sunlight into electricity [3]. This efficiency has improved significantly in the recent years, with the solar-cell efficiency rates increasing from 3.8% in 2009 to 25.2% in 2018 [4, 5]. Perovskites with a general formula ABX_3 [6, 7] have attracted a considerable interest due to their high stability and a tunable bandgap [8, 9]. Perovskites represent a class of materials with a unique crystal structure which makes them highly versatile for electronic and energy applications [10]. They have gained significant attention due to their excellent electronic properties, such as high carrier mobility [11] and photoelectric [12] and thermoelectric capabilities, [13] which make them ideal for such devices as solar cells, light-emitting diodes, [14] transistors [15] and photodetectors [16].

A hybrid organic–inorganic halide compound $CH_3NH_3PbI_3$ is one of the most well-known perovskites. It has shown an excellent performance in many photovoltaic applications due to its high light absorption and carrier mobility [17]. However, it has been found that the organic component of this perovskite can decompose under certain climatic conditions, thus leading to a release of harmful compounds into atmosphere [18, 19]. Furthermore, its inorganic component, Pb, is highly toxic, which

causes environmental and health concerns [20, 21]. As a result, the researchers in the field have been working on developing lead-free alternatives of $CH_3NH_3PbI_3$ that can maintain a high efficiency of perovskites. Germanium (Ge) and tin (Sn) have emerged as promising substitutes of Pb due to their similar oxidation states and properties. However, although they have a great potential, there are still challenges to be overcome in order to ensure their suitability while maintaining high efficiency. The researchers are also exploring some other possible alternatives to Pb, e.g. antimony (Sb), bismuth (Bi) and manganese (Mn), which have already shown promising results in the initial studies [22–26]. These elements have the electronic and optical properties similar to those of Pb, though they are less toxic and more environmentally friendly.

$RbGeX_3$ perovskites, with X = Cl, Br and I, have attracted a considerable interest of researchers due to their high stability and tunable bandgap. Several experimental and theoretical studies have revealed that the bandgap of these perovskite materials can be tuned by changing the halide ion. Therefore, studies of the electronic and optical properties of $RbGeX_3$ based on density functional theory (DFT) would be of significant interest for developing new optoelectronic devices [27]. In 2017, Z.-L. Yu et al. [28] have investigated the effect of strain engineering on the photovoltaic properties of γ-$RbGeX_3$ (X = Cl, Br and I) as a new class of halide perovskites with promising photovoltaic properties. Their results have demonstrated that strained γ-$RbGeX_3$ has a reduced bandgap and improved carrier-transport properties, which can be attributed to a changed strain-induced effective mass of electron. The authors have explained the underlying mechanism of this effect and suggested that their approach could be used to tune the electronic and optical properties of some other perovskite materials for photovoltaic applications. The authors have also highlighted potential advantages of strain engineering over the other approaches such as doping and alloying, since the latter techniques can introduce defects and impurities which could degrade the performance of a material.

The DFT calculations with a generalized gradient approximation (GGA) have been used to determine the optimized atomic positions, the lattice parameters, the electronic band structure and the density of states (DOS) of $RbGeCl_3$. In 2019, F. Erdinc et al. [29] have found that $RbGeCl_3$ is an indirect-bandgap semiconductor with the bandgap of 3.27 eV. This material is optically transparent with a high enough refractive index. It has a high reflectivity in the visible and infrared ranges. $RbGeCl_3$ represents a stiff material with a high elastic modulus, which makes it a potential candidate for the applications that require the materials with high strength and stiffness. In 2019, U.-G. Jong et al. [30] have performed the DFT calculations on Ge-based halide perovskites $AGeX_3$ (A=Cs, Rb; X= I, Br, Cl) with the rhombohedral unit cell and the space group R3m. The authors have observed that the lattice constants of these materials increase with increasing halogen-ion size, while the length of Ge–X bond decreases, thus indicating stronger bonding between Ge and halogen atoms. The Ge-based halide perovskites have been found to be thermodynamically stable, while their bandgap to decrease with increasing halogen-ion size. The valence-band (VB) maximum is dominated by the *p* orbitals of halogen atoms, while the conduction-band (CB) minimum is dominated by the *s* and *p* orbitals of Ge atoms. The optical properties of Ge-based halide perovskites have also been investigated. Their absorption coefficient and the refractive index have been found to increase with increasing halogen-ion size, which testifies that the above materials become more optically dense. In 2019, M. Houari et al. [31] have studied germanium iodide perovskites and their potential use in optoelectronic applications. The authors have employed the DFT calculations to find out the electronic and optical properties of three different $AGeI_3$ perovskites ($KGeI_3$, $RbGeI_3$ and $CsGeI_3$) at the ambient pressure. They have found that all of these perovskites have a direct bandgap which decreases as the size of the A cation increases. The absorption spectra of these perovskites extend into the visible range of electromagnetic

spectrum, thus indicating their potential use in the solar-cell applications. The above authors have also calculated the dielectric function, the refractive index and the reflectivity of each perovskite. They have observed that these characteristics vary with varying size of the A cation. This promotes further studies of the properties of $RbGeX_3$ and the ways to tune those properties.

It has been repeatedly demonstrated in a number of experimental and theoretical studies that the band structure (and so the bandgap and some other properties) of perovskites can be tuned by varying A, B and/or X components [32]. Nonetheless, the properties of perovskites can also be tuned by applying external fields, e.g. a hydrostatic pressure. Understanding the structural, electronic, optical and other properties of perovskites and the methods for tuning them are essential for developing new optoelectronic devices. There can be significant improvement in the properties of inorganic–inorganic and organic–inorganic perovskites subjected to a pressure. This can provide better results if compared with the common chemical or physical modifications. In particular, satisfactory achievements in the performance of metal halide perovskites subjected to high pressures have been observed, e.g. for the structural, electronic and optical properties. Simultaneous bandgap narrowing and increase in the lifetime of carriers have been detected for organic lead-halide perovskites $MAPbI_3$ (with MA denoting $[CH_3NH_3]^+$) and $FAPbI_3$ (with FA being formamidinium) under pressure [33–37]. A decrease in the bandgap and an enhancement in the emission and metallization have been predicted by the experiments. A high pressure improves the stability and the electrical conductivity of perovskite ($CH_3NH_3SnI_3$) [38]. Similar effects of pressure have also been observed in all-inorganic halide perovskites.

In 2022, S. K. Mitro et al. [39] have investigated the effect of pressure on the optoelectronic properties of lead-free halide perovskites $RbGeX_3$ (X = Cl and Br). The authors have utilized the DFT with the GGA and ultrasoft pseudo-potentials, using a CASTEP computational code. A 12×12×12 *k*-point grid has been employed in their simulations. The $RbGeCl_3$ and $RbGeBr_3$ materials have been subjected to the pressures ranging from 1 GPa to 10 GPa. At 6 GPa (for $RbGeCl_3$) and 4 GPa (for $RbGeBr_3$), the bandgap reaches a zero value. Unfortunately, the wavelength dependence of the absorption coefficient for these compounds has not been calculated in Ref. [39]. Application of the hydrostatic pressure to $CsSnCl_3$ causes a significant increase in the ductility, the optical absorption and the conductivity, as well as affects a semiconductor-to-metal transition [40]. So, semiconducting perovskite $CsYbF_3$ becomes metallic at 15 GPa [41].

To the best of our knowledge, the experimental results on $RbGeX_3$ under the hydrostatic pressure are still not available in the literature. In this work, we study theoretically the effect of hydrostatic pressure on the structure and photo-electronic properties of cubic perovskites $RbGeX_3$ (X = Cl, Br and I), using the *ab initio* calculations within the framework of the DFT. A 14×14×14 *k*-point grid is employed in our calculations, which provides more accurate results. Finally, the band structure, the total and partial densities of states (TDOS and PDOS), the imaginary and real components of the dielectric function, the refractive index and the absorption coefficient are calculated at different pressures.

2. Computational method

The unit cell of cubic perovskites $RbGeX_3$ (X = Cl, Br and I) belongs to the space group $Pm\bar{3}m$ (#221) and has five atoms that reside at the Wyckoff sites 1b (0.5 0.5 0.5) for Rb, 1a (0.0 0.0 0.0) for Ge and 3d (0.0 0.0 0.5) for X_3.

In the present work, we utilize a plane-wave pseudopotential (PW-PP) technique within the DFT, which is implemented the ABINIT package [42]. The GGA according to Perdew–Berg–Erzenhof (GGA-PBE) [43] is taken as the exchange-correlation term in the Kohn–Sham equations. In the framework of the PW-PP technique, the plane waves are, as usual, used as a basis set to

expand the wave functions. The norm-conserving, separable and dual-space Gaussian-type pseudopotentials by Goedecker, Teter and Hutter (GTH) [44] are considered to describe the valence electron–ion interaction. The valence states in the GTH approach are $4s^2\ 4p^6\ 5s^1$ for Rb, $4s^2\ 4p^2$ for Ge, $3s^2\ 3p^5$ for Cl, $4s^2\ 4p^5$ for Br, and $5s^2\ 5p^5$ for I [45].

Preliminary, convergence calculations were done, which resulted in the converged value 816.3 eV as a plane-wave cut-off energy at the Monkhorst–Pack [46] k-point mesh 6×6×6. Then, a structural geometry optimization of cubic $RbGeX_3$ (X = Cl, Br and I) was performed. The appropriate converged value, together with the optimized lattice constants and the relaxed atomic coordinates were used in all subsequent calculations. However, as the optical properties require a denser *k*-mesh, we used the mesh 14×14×14 for their computation. The geometry was optimized with the crystal subjected to different pressures. The band structures of $RbGeX_3$ (X = Cl, Br and I) under different pressures were calculated along the symmetry lines Γ (0.0 0.0 0.0)–X(0.5 0.0 0.0)–M(0.5 0.5 0.0)–R(0.5 0.5 0.5). The fundamental energy bandgap and the gaps at the other high-symmetry points were calculated. First, the band structures were calculated at the ambient pressure, $P = 0$. Then this was done for increasing pressure values, with the steps 1 GPa. Our results revealed that the fundamental bandgap becomes zero at the pressures 5.7, 3.5 and 3.3 GPa respectively for $RbGeCl_3$, $RbGeBr_3$ and $RbGeI_3$. Therefore, we were restricted to these pressures as upper limits. Then the TDOS and the PDOS were calculated at each pressure value.

Investigation of the optical properties requires the knowledge of frequency-dependent linear optical dielectric function. Here the spectra of the real and imaginary parts of the dielectric function and the other optical parameters were calculated with a density functional perturbation theory (DFPT) [47] and a well-known Kramers–Kronig relation [48]. The relevant procedures rely on computing the optical conductivity spectrum. The frequency-dependent optical conductivity $\sigma(\omega)$ is as follows:

$$\sigma(\omega) = \sigma_1(\omega) + i\sigma_2(\omega). \tag{1}$$

The real part $\sigma_1(\omega)$ of the optical conductivity can be obtained from a Kubo–Greenwood formula [49]

$$\sigma_1(\omega) = \frac{2\pi}{\Omega}\sum_{ij} F_{ij}\left|D_{ij}\right|^2 \delta\left(\epsilon_i - \epsilon_j - \omega\right), \tag{2}$$

where Ω is the unit cell volume and

$$F_{ij} = [F(\epsilon_i) - F(\epsilon_j)]/\omega, \tag{3}$$

with *F* being the Fermi–Dirac distribution. Here

$$D_{ij} = \frac{1}{3}\sum_{\alpha}\left|\psi_i|\nabla_\alpha|\psi_j\right|^2 \tag{4}$$

are the matrix elements of the velocity dipole, while ψ_i and ϵ_i are respectively the wave functions and the energy of the i^{th} Kohn–Sham orbital.

The imaginary part $\sigma_2(\omega)$ of the optical conductivity follows directly from the Kramers–Kronig relation:

$$\sigma_2(\omega) = -\frac{2}{\pi}C\int_0^\infty \frac{\sigma_1(\nu)\omega}{\left(\nu^2 - \omega^2\right)}d\nu, \tag{5}$$

where *C* is the principal value of the integral and ν denotes the frequency. Then the real and imaginary parts of the frequency-dependent dielectric function can be computed:

$$\varepsilon_1(\omega) = 1 - \frac{4\pi}{\omega}\sigma_2(\omega), \tag{6}$$

$$\varepsilon_2(\omega) = \frac{4\pi}{\omega}\sigma_1(\omega). \tag{7}$$

Here the dielectric function

$$\varepsilon(\omega) = \varepsilon_1(\omega) + i\varepsilon_2(\omega) \tag{8}$$

is given by

$$\varepsilon(\omega) = [n(\omega) + ik(\omega)]^2, \tag{9}$$

where $n(\omega)$ and $k(\omega)$ are the frequency-dependent refractive index and extinction coefficient, respectively. From Eqs. (11) and (12), one can obtain $n(\omega)$:

$$n(\omega) = \frac{1}{\sqrt{2}}\sqrt{|\varepsilon(\omega)| + \varepsilon_1(\omega)}. \tag{10}$$

Then the absorption coefficient $\alpha(\omega)$ can be derived using the relation

$$\alpha(\omega) = \frac{4\pi}{n(\omega)}\sigma_1(\omega). \tag{11}$$

The real and imaginary parts of the dielectric function, the refractive index and the absorption coefficient of $RbGeX_3$ (X = Cl, Br and I) were calculated for the incident photons with the energies from 0.008 to 43.527 eV under different pressures.

3. Result and discussion

3.1. Structural properties

Fig. 1 shows the crystal structure of cubic perovskites $RbGeX_3$ (X=Cl, Br and I). Due to the geometry optimization, one calculates the total energy of $RbGeX_3$ (X = Cl, Br and I) at different lattice constants (and, hence, different cell volumes), the plots of which are displayed in Fig. 2. The volume V_o of the unit cell and the lattice constant $a_o \equiv a$ corresponding to the minimum total energy E_o have been determined from this data. The a and E_o values obtained for the three compounds are listed in Table 1. They agree well with the theoretical results available in the literature. However, no experimental values are still present.

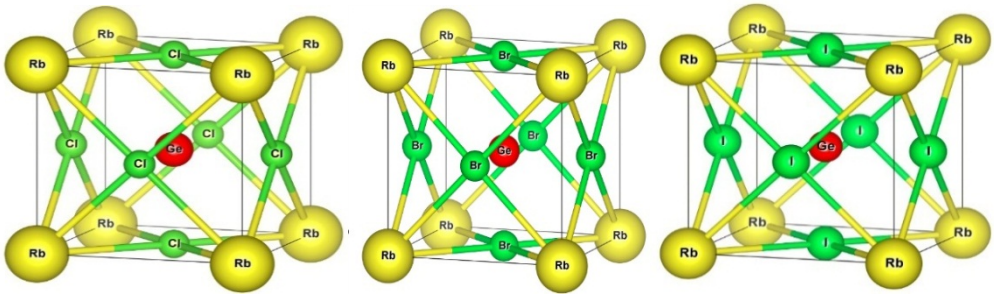

Fig. 1. Ideal cubic structure of $RbGeX_3$ (X = Cl, Br and I).

The variation of the total energy E with the unit-cell volume V has been fitted with a third-order Birch–Murnaghan equation of state [50]:

$$E(V) = E_0 + \frac{9V_0B_0}{16}\left\{\left[\left(\frac{V_0}{V}\right)^{\frac{2}{3}} - 1\right]^3 B_0' + \left[\left(\frac{V_0}{V}\right)^{\frac{2}{3}} - 1\right]^2\left[6 - 4\left(\frac{V_0}{V}\right)^{\frac{2}{3}}\right]\right\}, \tag{12}$$

where B_o and B_o' are respectively the bulk modulus and its pressure derivative, E_o implies the total energy and V_o the unit-cell volume [Note that all the parameters are referred to $P = 0$]. The B_o and B_o' values for the three compounds have been calculated from the fittings presented in Table 1. They agree well with the theoretical values available in the literature.

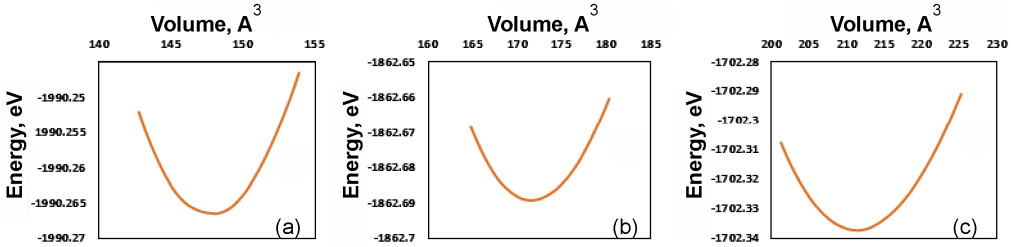

Fig. 2. Total energy against unit-cell volume, as calculated for (a) $RbGeCl_3$, (b) $RbGeBr_3$ and (c) $RbGeI_3$ at $P = 0$.

Interestingly, our results show that the bulk modulus of $RbGeCl_3$ is larger than those of $RbGeBr_3$ and $RbGeI_3$. Moreover, there is an inverse relationship between the bulk modulus and the atomic number of halogen atom, where the bulk modulus increases with decreasing density of perovskite. This trend could potentially be explained by the influence of halogen atom on bonding between Rb, Ge and the halogen atoms in the crystal lattice, which affects the overall stability and compressibility of the perovskite structure.

Table 1. Lattice constant a, bulk modulus B, pressure derivative B' of bulk modulus and total energy E_o calculated for $RbGeX_3$ (X = I, Br and Cl) at $P = 0$.

Compound	Data reference	a, Å	B, GPa	B'	E_o, eV
$RbGeCl_3$	Present work	5.286	26.892	3.953	–1990.266
	Experimental	n. a.	n. a.	n. a.	n. a.
	Theoretical	5.31 [51] 5.291 [39]	26.15 [51]	4.05 [51]	n. a.
$RbGeBr_3$	Present work	5.556	22.912	4.562	–1862.689
	Experimental	n. a.	n. a.	n. a.	n. a.
	Theoretical	5.57 [51] 5.563 [39]	22.48 [51]	4.14 [51]	n. a.
$RbGeI_3$	Present work	5.956	18.181	4.504	–1702.339
	Experimental	n. a.	n. a.	n. a.	n. a.
	Theoretical	5.97 [31]	12.58 [52]	n. a.	n. a.

The plots shown in Fig. 3 display the pressure dependences of the unit-cell volume for our compounds. They demonstrate clearly that increasing pressure decreases the unit-cell volume. In this study, different pressures have been applied to each compound until its bandgap reaches zero. Each perovskite had a unique pressure value at which this occurs. The lattice constants corresponding to the unit-cell volumes shown in Fig. 3 have been used in all subsequent calculations of the electronic and optical properties.

The lengths of the bond between the halogen atom and the Rb and Ge atoms for our $RbGeX_3$ (X = Cl, Br and I) compounds have also been calculated at different pressures ranging from $P = 0$ to P = metallization pressure. The results are demonstrated in Fig. 4. One can see from Fig. 4 that all the bond lengths decrease with increasing pressure.

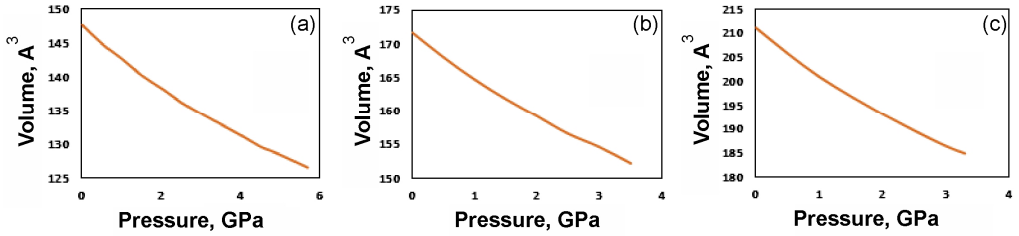

Fig. 3. Unit-cell volume versus hydrostatic pressure, as calculated for (a) $RbGeCl_3$, (b) $RbGeBr_3$ and (c) $RbGeI_3$.

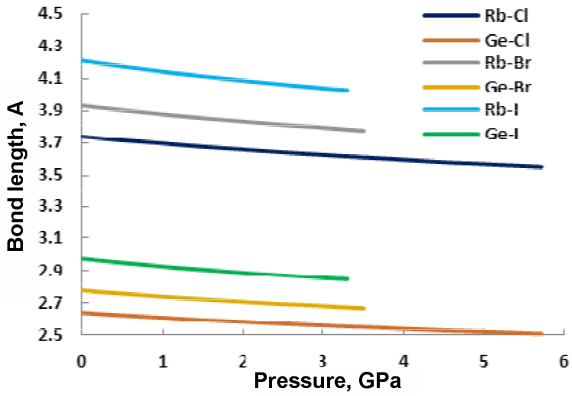

Fig. 4. Lengths of bonds between the halogen atom and the Rb and Ge atoms, as calculated for $RbGeX_3$ (X = Cl, Br and I) versus the hydrostatic pressure: the maximum pressures achieved correspond to metallization).

The total volume deformation potential $a_\upsilon^{\text{total}}$ due to hydrostatic pressure is given by the formula [53]

$$a_\upsilon^{total} = \frac{dE_{tot}}{d\ln V}, \tag{13}$$

where $d\ln V = \Delta V/V$. Here ΔV is the difference between the unit-cell volumes at P_1 and P_2, while V denotes the average of the two volumes [54].

We have calculated the total volume deformation potential $a_\upsilon^{\text{total}}$ due the pressure ranging from 0.5 to 3 GPa and from 0 up to the metallization pressure P_{metaliz} (see Table 2). Under the same pressure ($0.5 \rightarrow 3$ GPa), the response of $RbGeCl_3$ is stronger (i.e., the deformation potential is less) than that of $RbGeBr_3$ and $RbGeI_3$. Moreover, a relatively high pressure is required to metalize $RbGeCl_3$, a lower pressure is required for $RbGeBr_3$ and still less pressure for $RbGeI_3$. These different responses depend on how tightly the outermost halogen-*p* orbital (Cl-3*p*, Br-4*p* or I-5*p*) is bound to its atom. This will be discussed in a more detail in Section 3.3.

Table 2. Total volume deformation potentials calculated for $RbGeX_3$ (X = Cl, Br and I).

Compound	P_{metalliz}, GPa	a_υ^{total}, eV	
		$0.5 \rightarrow 3$ GPa	$0 \rightarrow P_{\text{metalliz}}$
$RbGeCl_3$	5.7	–1.509	–2.200
$RbGeBr_3$	3.5	–1.711	–1.649
$RbGeI_3$	3.3	–2.102	–1.562

3.2. Electronics properties

The band structure and the DOS are critical for understanding the electronic properties of a material. Replacing any atom in ABX_3 causes a change in its band structure. Obviously, this is due to different atomic numbers and, hence, different electronic configurations of the halogen atoms. Of course, a difference in the band structures means different properties. Application of the hydrostatic pressure also changes the band structure and, hence, the properties of a material.

By studying the band structures of $RbGeX_3$ (X = I, Br and Cl) under different pressures, one can find the pressure-induced changes in their properties. As a consequence, one can employ the pressure to tune these properties in different technological applications. The band structures of our perovskite compounds at different pressures are displayed in Figs. 5–7. At all the pressures, our compounds have a direct fundamental bandgap which is located at the symmetry point R.

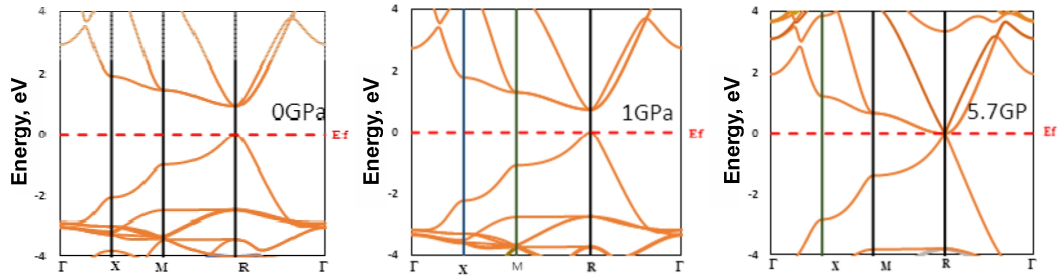

Fig. 5. Band structure of $RbGeCl_3$ under different pressures (see the legend).

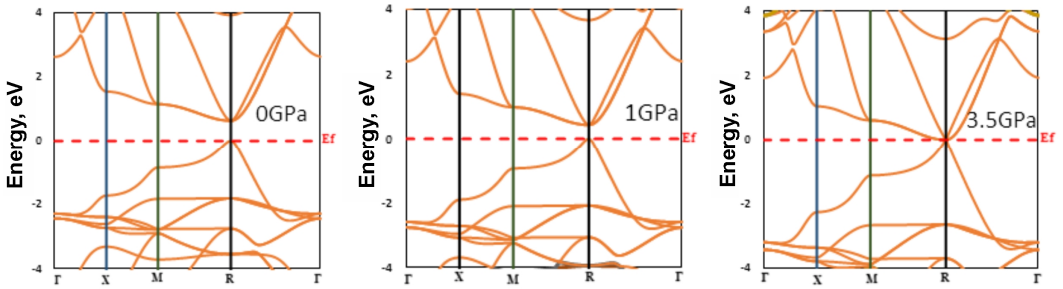

Fig. 6. Band structure of $RbGeBr_3$ under different pressures (see the legend).

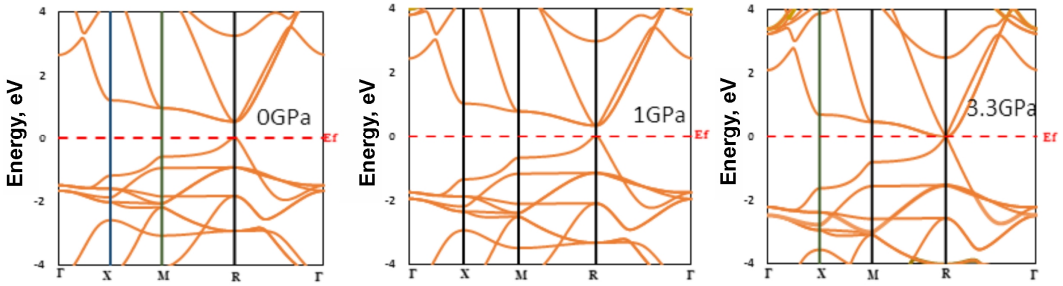

Fig. 7. Band structure of $RbGeI_3$ under different pressures (see the legend).

The fundamental bandgaps E^{R-R} for $RbGeCl_3$, $RbGeBr_3$ and $RbGeI_3$ calculated with the GGA-PBE approach at the ambient pressure $P = 0$ are equal respectively to 0.921, 0.63 and 0.545 eV. These values are in good agreement with the literature results (see Table 3). The bandgaps E^{M-M}, E^{X-X} and $E^{\Gamma-\Gamma}$ calculated respectively at the symmetry points M, X and Γ are also displayed in Table 3. Unfortunately, no results for a comparison are available for these points.

Table 3. Energy bandgaps E^{R-R}, E^{M-M}, E^{X-X} and $E^{\Gamma-\Gamma}$ calculated for $RbGeX_3$ (X= I, Br and Cl) under zero pressure.

Energy bandgap, eV						
E^{gap}	$RbGeCl_3$		$RbGeBr_3$		$RbGeI_3$	
	This work	Other works	This work	Other works	This work	Other works
E^{R-R}	0.9218	0.96 [51]	0.63176	0.67 [51]	0.54543	0.569 [31]
$E^{\Gamma-\Gamma}$	5.84185	n. a.	4.91519	n. a.	4.13371	n. a.
E^{X-X}	3.98334	n. a.	3.26877	n. a.	2.39767	n. a.
E^{M-M}	2.46125	n. a.	1.99425	n. a.	1.55841	n. a.

As seen from Figs. 5–7, the replacement, at a given pressure, of the halogen atom Cl by Br and then by I in $RbGeX_3$ changes the band structure and so the properties. Obviously, this is due to different atomic numbers and electron configurations of the halogen atoms. Moreover, Figs. 5–7 reveal the changes in the band structure of each of our compounds occurring with changing pressure.

By changing the halogen atom, one can control the band structure and the DOS. For example, this enables tuning the bandgap value to meet specific technological requirements. These findings can have significant implications in the design of optoelectronic devices such as solar cells and light-emitting diodes, where the bandgap is a crucial parameter that determines the performance of a device.

It is worth reminding that the ranges of pressures applied to different $RbGeX_3$ (X = Cl, Br and I) compounds are not the same. This is a consequence of the fact that the pressure at which the bandgap value becomes zero is different for different compounds. The bandgap becomes zero at 5.7 GPa for $RbGeCl_3$, at 3.5 GPa for $RbGeBr_3$ and at 3.3 GPa for $RbGeI_3$. Therefore, $RbGeCl_3$, $RbGeBr_3$ and $RbGeI_3$ have been subjected to the pressures respectively in the ranges 1.0–5.7, 1.0–3.5 and 1.0–3.3 GPa. In other words, we have demonstrated that cubic $RbGeCl_3$, $RbGeBr_3$ and $RbGeI_3$ crystals are transformed from semiconductors into conductors at the pressures 5.7, 3.5 and 3.3 GPa, respectively. This phenomenon has a potential for various applications, including a development of pressure sensors and manipulations of the electronic properties of materials.

The pressure changes taking place with the energy bandgaps E^{R-R}, E^{M-M}, E^{X-X} and $E^{\Gamma-\Gamma}$ are plotted in Fig. 8. It is evident that the pressure imposes notable changes in the bandgap values referred to the high-symmetry *k*-points. The bandgap energy $E_g^{\Gamma\text{-}\Gamma}$ at the point Γ increases with increasing pressure. The bandgap $E_g^{\text{X-X}}$ at the X point almost does not change under the same condition. This could indicate that the electronic structure of $RbGeX_3$ at the symmetry point X are less sensitive to the pressure changes, if compared to that occurring at the Γ point. The energy bandgap at the M point, $E_g^{\text{M-M}}$, decreases slightly with increasing pressure. Finally, the fundamental bandgap $E_g^{\text{R-R}}$ experiences the most significant decrease with increasing pressure.

The energies of the transitions occurring across the main gaps are functions of pressure. The pressure dependences of the calculated gaps $E_g^{\text{R-R}}$, $E_g^{\text{M-M}}$, $E_g^{\Gamma\text{-}\Gamma}$ and $E_g^{\text{X-X}}$ have been obtained using the least-squares method. In the case of $RbGeCl_3$, they can be represented as follows:

$$E^{\text{R–R}}(P) = -0.161318P + 0.902251 \ (R^2 = 0.9981), \quad (14)$$

$$E^{\text{M–M}}(P) = -0.068181P + 2.458905 \ (R^2 = 0.9997), \quad (15)$$

$$E^{\text{G–G}}(P) = 0.068871P + 5.854515 \ (R^2 = 0.9961), \quad (16)$$

$$E^{\text{X–X}}(P) = -0.00374P^2 + 0.032494P + 3.985241 \ (R^2 = 0.9929), \quad (17)$$

$$E^{\text{X–X}}(P) = 0.010910P + 4.002269 \ (R^2 = 0.7611), \quad (18)$$

where E is in eV and T is in GPa. The same is true for other equations.

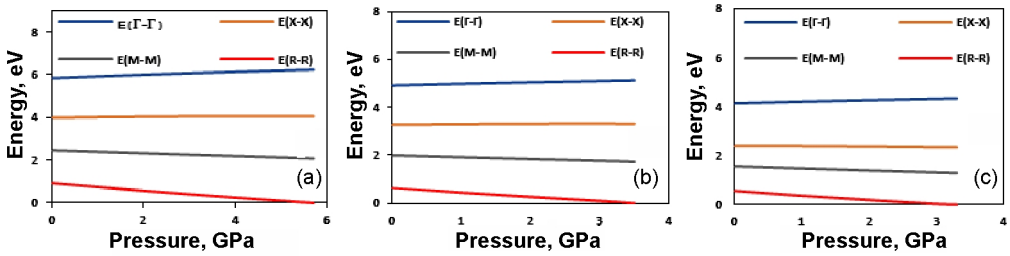

Fig. 8. Pressure dependences of energy bandgaps E^{R-R}, E^{M-M}, E^{X-X} and $E^{\Gamma-\Gamma}$ calculated for (a) $RbGeCl_3$ (b) $RbGeBr_3$ and (c) $RbGeI_3$.

All the $E(P)$ dependences are linear functions of the pressure P, except for the $E^{X–X}(P)$ one for which, according to the R^2 value, a quadratic equation represents a better fit. It is clear from Eqs. (14)–(17) that the pressure change in the $E^{R–R}$ parameter (–161.318 meV/GPa) is more significant than those of the other parameters. On the other hand, the $E^{X–X}(P)$ dependence is the weakest.

Considering a linear pressure dependence of the fundamental energy gap $E^{R–R}$ for $RbGeCl_3$ (see Eq. (14)), one can obtain the metallization pressure 5.593 GPa. On the other hand, one can also consider the more exact quadratic function:

$$E^{R–R}(P) = 0.0043704P^2 - 0.1865104P + 0.92212574 (R^2 = 0.9999). \quad (19)$$

Then we have $E^{R–R} = 0$ at $P = 5.69902$ GPa, which is much closer to the metallization pressure 5.7 GPa predicted from the direct band-structure calculations (see Fig. 4). Thus, one concludes that, as far as the metallization pressure is concerned, Eq. (19) is a better approximation for the $E^{R–R}(P)$ function of $RbGeCl_3$.

For $RbGeBr_3$ and $RbGeI_3$, we consider only the functions $E^{R–R}(P)$. They can be described respectively as

$$E^{R–R}(P) = -0.178343P + 0.620681 (R^2 = 0.9985) \quad (20)$$

and

$$E^{R–R}(P) = -0.1662701P + 0.531715 (R^2 = 0.9961). \quad (21)$$

From Eqs. (20) and (21), one can derive the metallization pressures for $RbGeBr_3$ and $RbGeI_3$, which are equal respectively to 3.4803 and 3.1979 GPa.

3.3. Density of states

The focus of the current study is the electronic properties under different pressures, a task for which the knowledge of the TDOS and the PDOS is essential. We have calculated the TDOS and PDOS functions for the cubic crystals $RbGeX_3$ (X = Cl, Br and I) at different pressures. Figs. 9–11 display these dependences for three different pressures only. They provide a comprehensive picture of the changes occurring in the number of electron states with increasing pressure and offer a valuable insight into the behaviour of our materials under compression.

For all of our $RbGeX_3$ (X = Cl, Br and I) perovskites, the PDOS demonstrate that the lower-energy (< –5 eV) region of the VB arises notably from the contributions of Rb-4*p*, Ge-4*s* and halogen-atom *s*-orbitals and involves a small contribution from Ge-4*p* orbital. The higher-energy VB region (> –5 eV) arises mainly from the large contributions of Ge-4*p*, Ge-4*s* and halogen-atom *p*-orbitals. Here the contribution of the halogen *p*-orbital is the largest. At the same time, the Rb-4*d* and Ge-3*d* orbitals contribute insignificantly. The same trend takes place at all the pressures. The *s*, *p* and *d* orbitals of both Rb and Ge mainly form the CB, with the Rb-4*d* orbitals having a greater

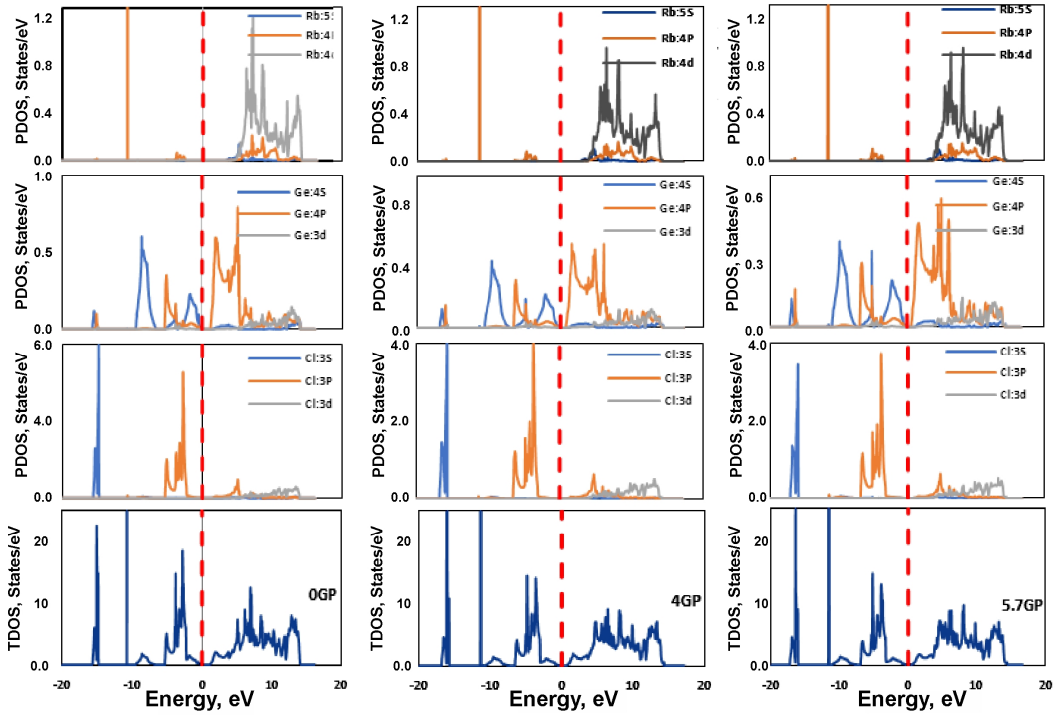

Fig. 9. TDOS and PDOS calculated for $RbGeCl_3$ at three different pressures (see the legend). Red dashed line indicates the Fermi level.

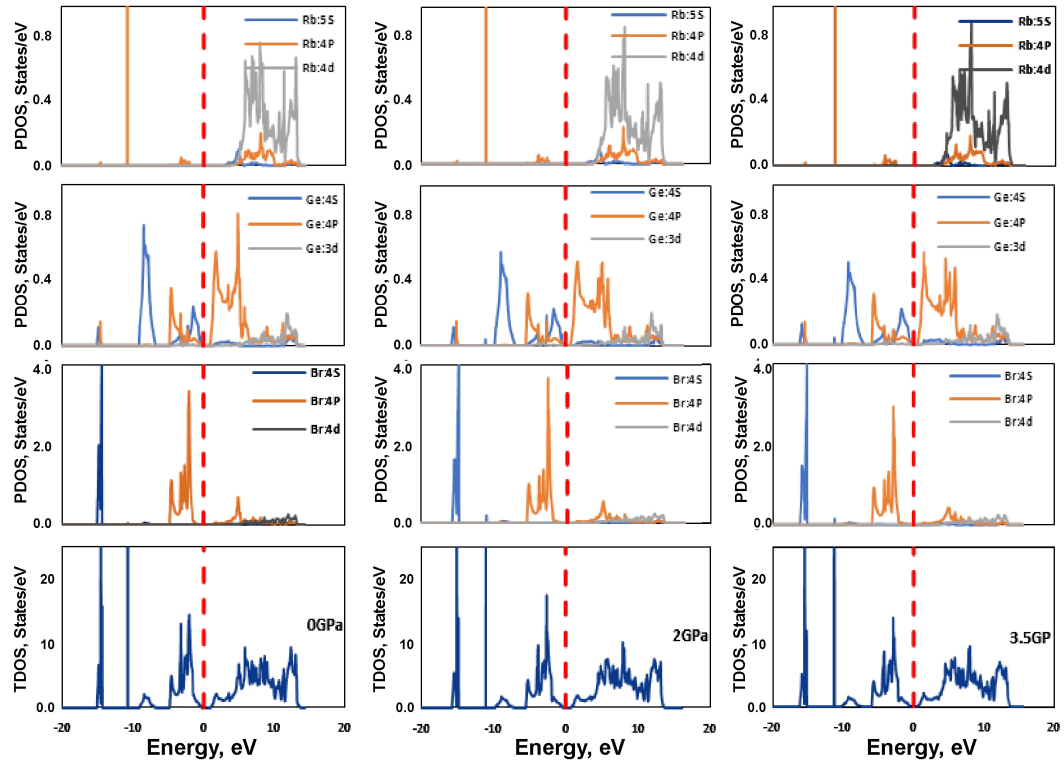

Fig. 10. TDOS and PDOS calculated for $RbGeBr_3$ at three different pressures (see the legend). Red dashed line indicates the Fermi level.

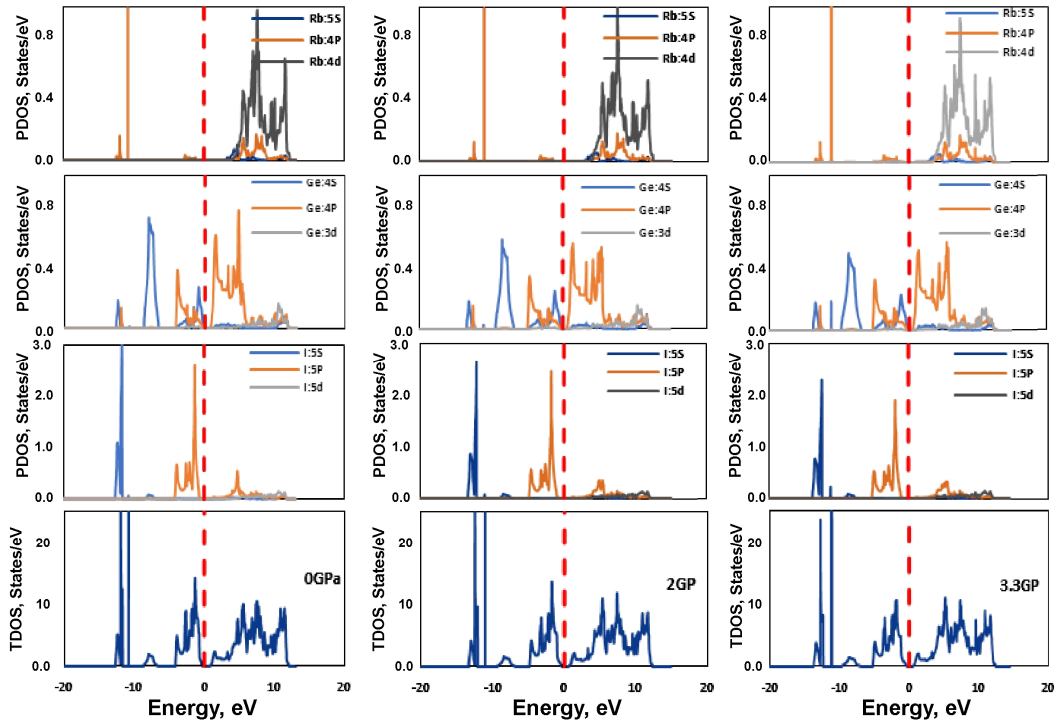

Fig. 11. TDOS and PDOS calculated for $RbGeI_3$ at three different pressures (see the legend). Red dashed line indicates the Fermi level.

role. The contributions of the *p* and *d* orbitals of the halogen atom are much less, while the ones related to the *s* orbital are almost insignificant. The higher-energy region of the CB arises mostly from the Rb-4*d* orbital, while its lower-energy region is formed by the Ge-4*p* orbital. The PDOS curves for the three halogen atoms Cl, Br and I are close to each other, so that their replacements have no essential effect. However, the TDOS in the high-energy VB region (~ –2 eV) is larger at 2 GPa, especially for $RbGeBr_3$. Clearly, the pressure makes the VB and the CB closer to each other and so enhances the electron transitions into the CB, thereby improving the conductivity.

Our calculations of the PDOS reveal that the edge of the VB for $RbGeCl_3$, $RbGeBr_3$ and $RbGeI_3$ mainly arises from the 3*p*-orbitals of Cl, the 4*p*-orbital of Br and the 5*p*-orbital of I, respectively. The edge of the CB for these compounds is mainly due to the 4*p*-orbital of Ge (see Figs. 9–11). This implies that the R–R energy gap arises from the difference between the 4*p*-orbital of Ge atom and the *p*-orbital of halogen atom (Cl-3*p*, Br-4*p* and I-5*p*). Thus, the first transition occurring from the VB into the CB is the transition from the halogen-*p* orbital to the Ge-4*p* orbital. Figs. 9–11 also reveal that, as the pressure increases, the 4*p*-orbital of Ge is pulled down and the *p*-orbital of the halogen atom (Cl-3*p*, Br-4*p* and I-5*p*) is pulled up on the energy scale. This reduces the R–R gap till the orbitals mentioned above overlap at a certain pressure (i.e., the metallization pressure). In other words, it is the effect of pressure on the Ge-4*p* and halogen-*p* orbitals that causes the metallization effect.

The effect of pressure on the R–R energy gap of our compounds obviously depends on how tightly the uppermost halogen-*p* orbital (Cl-3*p*, Br-4*p* and I-5*p*) is bound to its atom. The 3*p*-orbital of Cl is tighter (i.e., it has a lower orbital energy) than the 4*p*-orbital of Br which, in its turn, is tighter than the 5*p*-orbital of I. Hence, the response of the 3*p*-orbital of Cl to the pressure is stronger than that of the 4*p*-orbital of Br which, in its turn, is stronger than that of the 5*p*-orbital of I. Consequently,

$RbGeCl_3$ has to be metalized at a higher pressure when compared to $RbGeBr_3$ and $RbGeI_3$, and $RbGeBr_3$ at a higher pressure when compared to $RbGeI_3$. This is confirmed by our results: we remind again that the metallization pressures for $RbGeCl_3$, $RbGeBr_3$ and $RbGeI_3$ amount respectively to 5.7, 3.5 and 3.3 GPa.

To illustrate better the effect of pressure, in Fig. 12 we plot together the TDOS curves for $RbGeX_3$ (X = Cl, Br and I) under different pressures. It is evident that the effect of pressure is significant. Moreover, the TDOS curves shift towards higher energies and the upper VB shift is greater than that of the CB. Thus, the fundamental bandgap decreases with increasing pressure, reaching eventually a zero value.

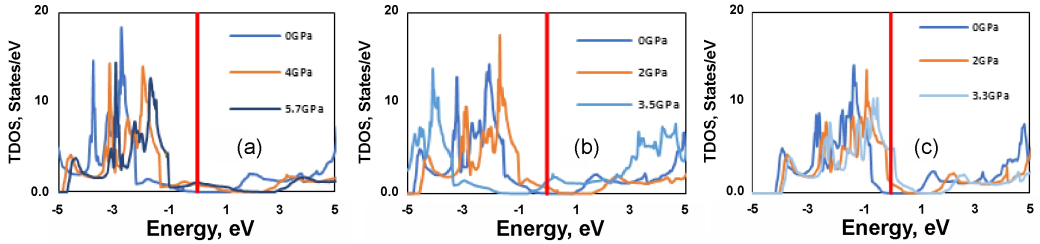

Fig. 12. TDOS curves calculated for (a) $RbGeCl_3$, (b) $RbGeBr_3$ and (c) $RbGeI_3$ under different pressures. Red solid line indicates the Fermi level.

3.4. Optical properties

We have calculated the imaginary parts $\varepsilon_2(\omega)$ of the dielectric function for $RbGeX_3$ (X = Cl, Br and I) as functions of the photon energy under different pressures. They are displayed in Fig. 13. Here the panels (a) and (b) show the imaginary parts of the dielectric functions for three different pressures, while the panel (c) refers to five pressure values. The effect of pressure on the $\varepsilon_2(\omega)$ spectra of our compounds is in accordance with its effect on the fundamental energy bandgap. In particular, we have $\varepsilon_2 = 0$ for the photon energies less than the gap width. For instance, the spectra at the zero pressure start at approximately 0.9, 0.6 and 0.5 eV respectively for $RbGeCl_3$, $RbGeBr_3$ and $RbGeI_3$ (see the E^{R-R} values gathered in Table 3). When the pressure increases, the ε_2 spectra exhibit a shift towards lower photon energies, as a response to the bandgap decrease occurring with increasing pressure.

There are four distinct peaks in the ε_2 spectra calculated for $RbGeCl_3$ (see Fig. 13a). The peak (1) is close to 2 eV. Consulting with the PDOS data (see Fig. 9), one can notice that it corresponds to the 4*s*-Ge- and 4*p*-Ge-orbital energies. This is why the peak (1) arises from the electron transitions occurring from the 4*s* orbital of Ge to the 4*p* orbital of Ge. The peak (2) comes from the jumps of electrons from the 3*p* orbital of Cl to the 4*d* orbital of Rb. The relevant peak position is 9 eV, which corresponds to the energy of 3*p*-Cl and Rb-4*d* orbitals (see Fig. 9). The peak (3) originates from the electrons that leave the 4*p* orbital of Rb in the VB and move to the 4*p* orbital of Ge. This peak is located close to the photon energy 12 eV. Finally, the peak (4) appears due to the electron transitions occurring from the 4*p* orbital of Rb and the 3*p* orbital of Cl to the 4*d* level of Rb and the 4*p* level of Ge. The same is valid for $RbGeBr_3$ and $RbGeI_3$.

A novel observation made in our work is an inverse relationship between the bandgap and the imaginary part of the dielectric function $\varepsilon_2(\omega)$, which holds true for our compounds. Clearly, an increase in the pressure applied to our perovskites leads to decrease in their bandgap. In its turn, this results in increasing imaginary part of the dielectric function, as depicted in Fig. 13. The

imaginary part of the dielectric function is closely related to the band structure of a material and provides a detailed explanation of its absorption properties. The maximums of the imaginary part of the dielectric function vary with pressure: they increase notably in the infrared and visible ranges with increasing pressure. Beyond the visible range, the imaginary part of the dielectric function decreases. At high enough photon energies (> 20 eV), the imaginary part of the dielectric function for cubic perovskites $RbGeX_3$ (X = Cl, Br and I) becomes almost zero at all the pressures under test.

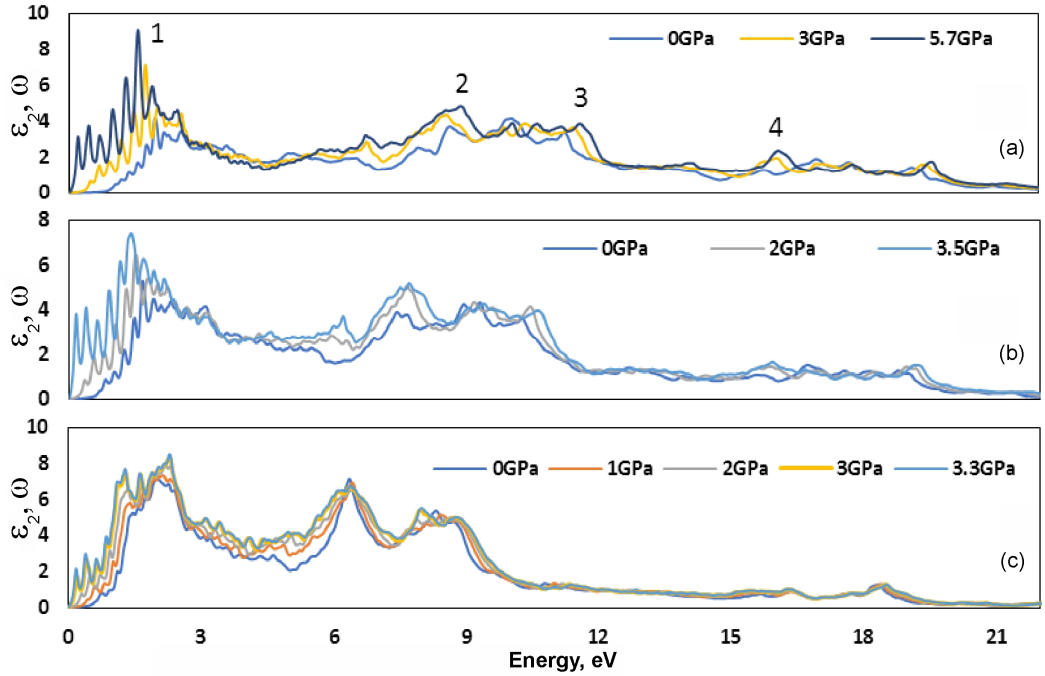

Fig. 13. Spectra of imaginary parts of the dielectric functions calculated for (a) $RbGeCl_3$, (b) $RbGeBr_3$ and (c) $RbGeI_3$ under different pressures (see the legend).

Fig. 14 shows the spectra of the real part $\varepsilon_1(\omega)$ of the dielectric function for our compounds, which are plotted against the photon energy at different pressures. At the ambient pressure, the zero-frequency limit increases as the halogen changes from Cl to I. The maximum $\varepsilon_1(\omega)$ values occur at around 2 eV for $RbGeCl_3$ and $RbGeBr_3$ and at around 1 eV for $RbGeI_3$. The $\varepsilon_1(\omega)$ values become close to zero at the photon energies 11.2, 10.2 and 8.3 eV respectively for $RbGeCl_3$, $RbGeBr_3$ and $RbGeI_3$. Beyond these energy regions, $\varepsilon_1(\omega)$ becomes negative, thus resulting in a higher reflectivity. Finally, the real parts of the dielectric functions for our compounds approach a unit value above 20 eV, which causes the materials to become transparent for the high-energy radiation [41].

The static dielectric constant $\varepsilon_1(0)$ (see Table 4) and its dependence on the pressure and the energy bandgap in $RbGeX_3$ (X = Cl, Br and I) represents a novel research area which can provide an insight into the electronic and optical properties of these materials. The facts that the static dielectric constant increases with increasing pressure and is inversely related to the bandgap are a unique characteristic of our perovskites, which has been rarely observed in the other materials. The shift of the $\varepsilon_1(0)$ maximums towards lower photon energies with increasing pressure is also a noteworthy observation. This shift points to a change occurring in the electronic and optical properties of our materials with changing pressure, which can be a finding important for the

development of pressure-dependent optoelectronic devices. We emphasize that a smaller bandgap of $RbGeI_3$, if compared with the other two perovskites, and the fact that the real part of its dielectric constant becomes zero 'sooner' than those of $RbGeCl_3$ and $RbGeBr_3$ are unique characteristics of the $RbGeI_3$ material which has not yet been reported in the literature.

Table 4. Static dielectric constant, refractive index, maximal real part of the dielectric function and maximal refractive index of $RbGeCl_3$, $RbGeBr_3$ and $RbGeI_3$, as calculated at the ambient pressure. The frequencies ν of incident photons corresponding to the maximums are also given.

Compound	$\varepsilon_1(0)$	$n(0)$	$\varepsilon_{1max}(\omega)$	ν, 10^{14} Hz	$n_{max}(\omega)$	ν, 10^{14} Hz
$RbGeCl_3$	4.999528	2.235962	6.663053	4.11	2.647554	4.60
$RbGeBr_3$	6.260382	2.502075	8.468158	3.41	2.946714	3.43
$RbGeI_3$	7.718804	2.778274	10.64287	2.96	3.291855	2.98

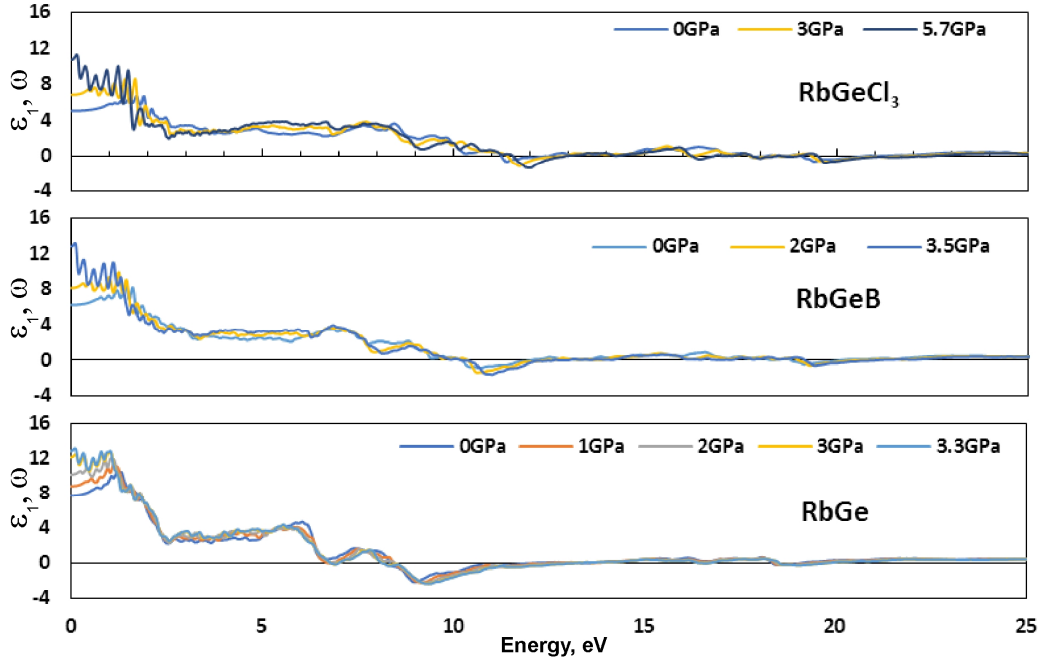

Fig. 14. Spectra of real parts of the dielectric functions calculated for $RbGeX_3$ (X = Cl, Br and I) under different pressures (see the legend).

The behaviour of the refractive-index spectra is similar to that observed for the real part of the dielectric constant. Fig. 15 shows the dependences of the refractive index $n(\omega)$ of $RbGeX_3$ (X = Cl, Br and I) on the photon energy. The refractive index increases if we pass from Cl to I (see Table 4). Moreover, Fig. 15 demonstrates that the refractive index increases with increasing pressure.

At 0 GPa, the zero limit of frequency refractive indices $n(0)$ of $RbGeI_3$, $RbGeBr_3$ and $RbGeCl_3$ are equal respectively to 2.7, 2.5 and 2.2. Fig. 15 demonstrates that the refractive indices of $RbGeCl_3$, $RbGeBr_3$ and $RbGeI_3$ increase with increasing energy of incident photons. At the ambient pressure, they acquire their maximums at 1.90, 1.42 and 1.23 eV respectively for $RbGeCl_3$, $RbGeBr_3$ and $RbGeI_3$ (see Table 4). They decrease gradually to unity around the energies 11.4, 10.6 and 9.0 eV and then go below unity at still higher photon energies. Note that the significance of the refractive index at the zero frequency is little since it is the same as the refractive index observed at very low frequencies. There is no sudden change in the refractive index just because the frequency becomes

zero. Indeed, the refractive index is defined as a factor by which an electromagnetic wave slows down if compared to the light speed c in a vacuum. This enables the calculation of the velocity υ of an electromagnetic wave according to the formula $\upsilon = c / n$. The only possibility for the n value to become less than unity is when the phase velocity υ in a material medium exceeds the light speed c. This would not violate the special relativity theory since the wave does not penetrate into the material and so carries no energy or information. In other words, a phase velocity exceeding c does not mean the propagation of signals with the velocities above c [55].

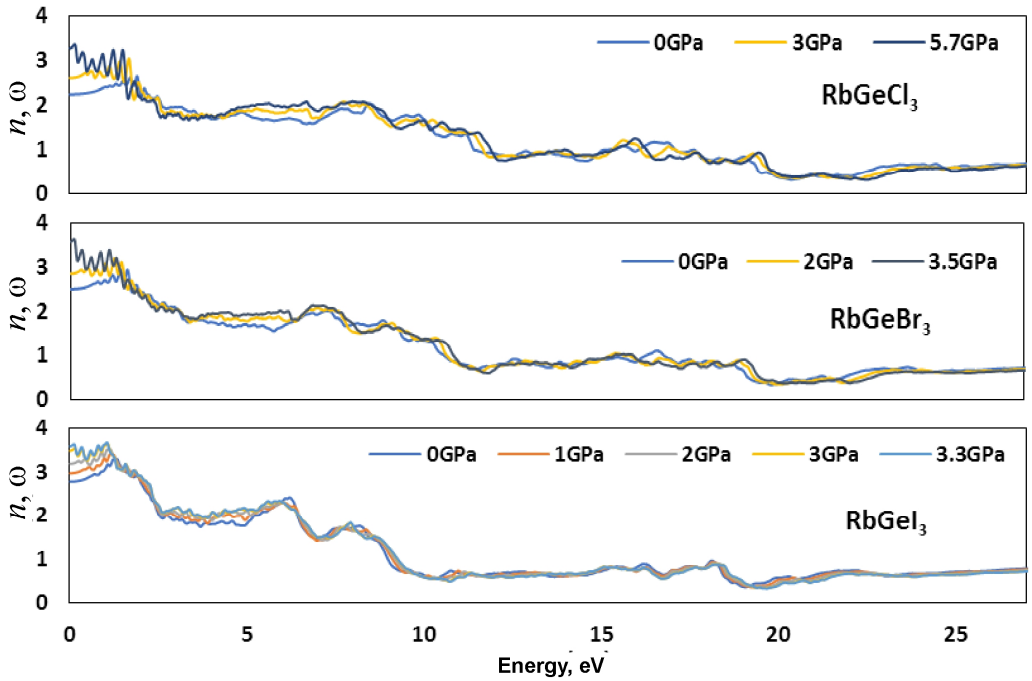

Fig. 15. Refractive-index spectra calculated for $RbGeX_3$ (X = Cl, Br and I) under different pressures (see the legend).

The absorption provides distinctive information about the ability of a material to convert solar energy and becomes important in such practical fields as solar-cell production or electromagnetic cells devices. The absorption spectra of $RbGeX_3$ (X = Cl, Br and I) plotted versus the photon energy at different pressures are shown in Fig. 16. Note that the absorption edges for $RbGeI_3$, $RbGeBr_3$ and $RbGeCl_3$ start respectively at 0.5, 0.6 and 0.9 eV. The absorption coefficients obtained for our perovskites conform well to the bandgap values calculated from the electronic band structure. This observation confirms the reliability of our results. The same is also true for the imaginary part of the dielectric constant. According to Fig. 16, the highest peaks observed for $RbGeI_3$, $RbGeBr_3$ and $RbGeCl_3$ are equal respectively to 1.64×10^8, 1.73×10^8 and 1.96×10^8 m^{-1}. They are located at the photon energies 8.922, 19.10 and 19.388 eV, respectively. These peaks correspond to the highest absorption of light energy. It is clear that the peaks change notably when we pass from Cl to I. In addition to the role of halogen atoms in the changes observed in the peak positions and magnitudes, the pressure also affects these peaks.

Fig. 16 testifies that our perovskites have a high absorption. This behaviour makes these materials useful for the solar-energy technologies. In addition, we have found that the pressure changes significantly the absorbance of our perovskites, which is accompanied with only slight

changes in their energy levels. This evidences that the pressure can control efficiently the absorption of our materials. Therefore, the hydrostatic pressure can be considered as an important factor which makes the perovskites under study useful for different applications.

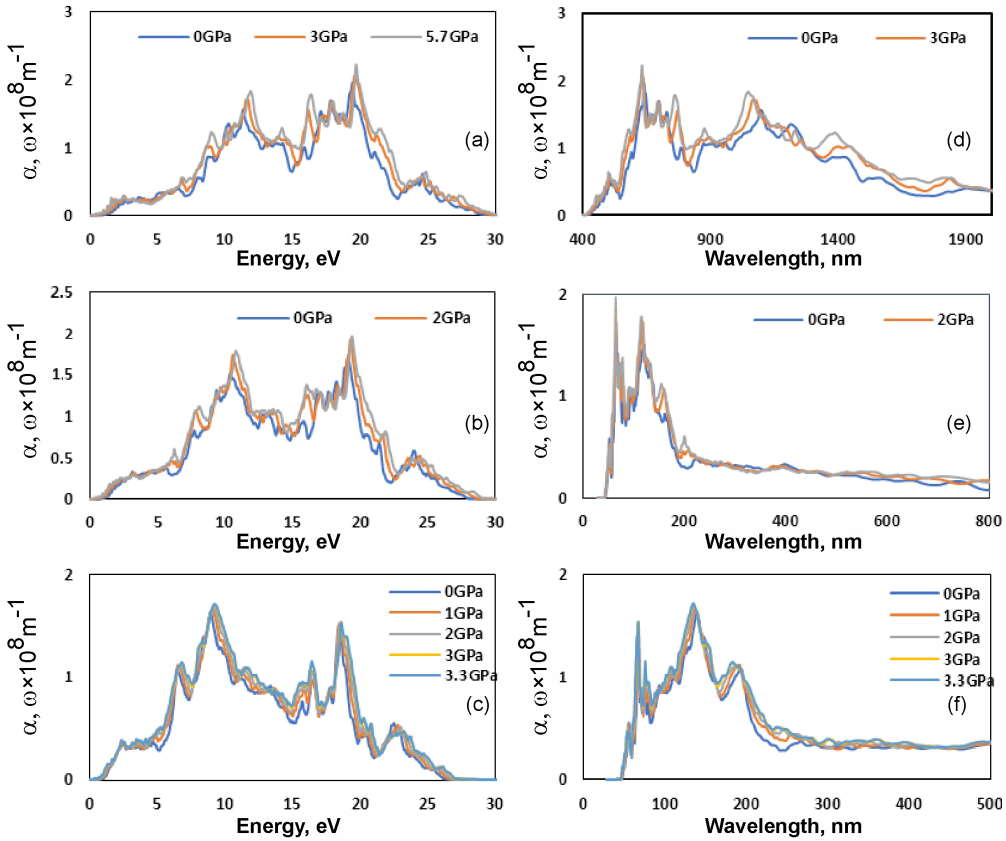

Fig. 16. Left panels: dependences of absorption coefficients for (a) $RbGeCl_3$, (b) $RbGeBr_3$ and (c) $RbGeI_3$ on the photon energy. Right panels: dependences of absorption coefficients for (d) $RbGeCl_3$, (e) $RbGeBr_3$ and (f) $RbGeI_3$ on the light wavelength. The pressures are indicated in the legend.

For further understanding of the optical properties of our perovskites, we plot the wavelength dependences of the absorption coefficients for $RbGeX_3$ in right-hand panels of Fig. 16. It is clear that $RbGeCl_3$ has a maximal-absorption peak in the visible range (from around 600 to 700 nm). $RbGeBr_3$ and $RbGeI_3$ have the appropriate peaks in the region 100–200 nm, which corresponds to invisible light. One can also note from Fig. 16 that the absorption of $RbGeX_3$ (X = Br, Cl and I) increases with increasing pressure.

4. Conclusions

The structural, electronic and optical properties of inorganic lead-free halide perovskites $RbGeX_3$ (X = Cl, Br and I) have been theoretically studied under hydrostatic pressure, using the PBE approach with the GGA exchange-correlation energy in the framework of the DFT. Our studies reveal that all the three perovskite compounds have a direct bandgap at the high-symmetry k-point R and the bandgap decreases with increasing pressure.

The optical properties of $RbGeX_3$ have been calculated using the DFPT approach and the Kramers–Kronig relation. The refractive index and the absorption coefficient of our compounds increase and get shifted towards higher photon energies when the pressure increases. Similar

changes are also observed if we change the halogen atom from Cl to I, except for that the appropriate shift is towards lower photon energies. At the ambient pressure, $RbGeCl_3$, $RbGeBr_3$ and $RbGeI_3$ acquire a metallic response to photons respectively in the energy regions 11.2–12.5, 10.2–12.0 and 8.3–12.2 eV. The above regions become shifted towards higher photon energies with increasing pressure. A similar metallic behaviour is observed at some photon energies located around 16 and 19.5 eV.

The zero-frequency limit of the refractive index increases with increasing pressure for all the three perovskites. At a given pressure, it also increases when we replace the halogen Cl atom by the I atom. The absorption coefficient is high enough in the visible range and becomes about four times higher at the low photon energies inside the ultraviolet range. The absorption coefficient becomes zero at higher photon energies (> 25 eV).

Finally, we stress that our first-principles study of the structural, electronic and optical properties of $RbGeX_3$ (X = Cl, Br and I) perovskites under the hydrostatic pressure can facilitate further fundamental researches and a development of new optoelectronic devices, photonic applications and solar-cell technology.

Acknowledgement

The authors would like to thank the co-workers of the Physics Department of the University of Zakho for their assistance in completion of this work.

References

1. Green M A, Ho-Baillie A and Snaith H J, 2014. The emergence of perovskite solar cells. Nature Photon. **8**: 506–514.
2. Ašmontas S, Čerškus A, Gradauskas J, Grigucevičienė A, Juškėnas R, Leinartas K, Lučun A, Petrauskas K, Selskis A, Sužiedėlis A and Širmulis E, 2022. Impact of cesium concentration on optoelectronic properties of metal halide perovskites. Mater. **15**: 1936.
3. Liang C, Gu H, Xia J, Mei S, Pang P, Zhang N, Guo J, Guo R, Shen Y, Yang S, Wei Z, Shao G and Xing G, 2022. Recent progress in perovskite-based reversible photon-electricity conversion devices. Adv. Func. Mater. **32**: 2108926.
4. Kojima A, Teshima K, Shirai Y and Miyasaka T, 2009. Organometal halide perovskites as visible-light sensitizers for photovoltaic cells. J. Amer. Chem. Soc. **131**: 6050–6051.
5. Sahli F, Werner J, Kamino A B, Bräuninger M, Monnard R, Paviet-Salomon B, Barraud L, Ding L, Diaz Leon J J, Sacchetto D, Cattaneo G, Despeisse M, Boccard M, Nicolay S, Jeangros Q, Niesen B and Ballif C, 2018. Fully textured monolithic perovskite/silicon tandem solar cells with 25.2% power conversion efficiency. Nature Mater. **17**: 820–826.
6. Johnsson M and Lemmens P. Crystallography and Chemistry of Perovskites. arXiv Preprint cond-mat/0506606, 2005.
7. Demic S, Ozcivan A N, Can M, Ozbek C and Karakaya M, Recent progresses in perovskite solar cells. In Nanostructured Solar Cells Ed. by N.Das, InTech: Rijeka, 277–304 (2017).
8. Li Z, Yang M, Park J-S, Wei S-H, Berry J J and Zhu K, 2016. Stabilizing perovskite structures by tuning tolerance factor: formation of formamidinium and cesium lead iodide solid-state alloys. Chem. Mater. **28**: 284–292.
9. Sutton R J, Eperon G E, Miranda L, Parrott E S, Kamino B A, Patel J B, Hörantner M T, Johnston M B, Haghighirad A A, Moore D T and Snaith H J, 2016. Bandgap-tunable cesium lead halide perovskites with high thermal stability for efficient solar cells. Adv. Energy Mater. **6**: 1502458.

10. Zhang W, Eperon G E and Snaith H J, 2016. Metal halide perovskites for energy applications. Nature Energy. **1**: 1–8.
11. Herz L M, 2017. Charge-carrier mobilities in metal halide perovskites: fundamental mechanisms and limits. ACS Energy Lett. **2**: 1539–1548.
12. Ji Y, Xu W, Rasskazov L L, Liu H, Hu J, Liu M, Zhou D, Bai X, Agren H and Song H, 2022. Perovskite photonic crystal photoelectric devices. Appl. Phys. Rev. **9**: 041319.
13. Wu T and Gao P, 2018. Development of perovskite-type materials for thermoelectric application. Mater. **11**: 999.
14. Wei Z and Xing J, 2019. The rise of perovskite light-emitting diodes. J. Phys. Chem. Lett. **10**: 3035–3042.
15. Liu A, Zhu H, Bai S, Reo Y, Zou T, Kim M-G and Noh Y-Y, 2022. High-performance inorganic metal halide perovskite transistors. Nature Electron. **5**: 78–83.
16. Li Y, Shi Z-F, Li X-J and Shan C-X, 2019. Photodetectors based on inorganic halide perovskites: Materials and devices. Chin. Phys. B. **28**: 017803.
17. Jonathan L, Diguna L J, Samy O, Muqoyyanah M, Bakar A S, Birowosuto M D and El Moutaouakil A, 2022. Hybrid organic–inorganic perovskite halide materials for photovoltaics towards their commercialization. Polymers. **14**: 1059.
18. Ma L, Guo D, Li M, Wang C, Zhou Z, Zhao X, Zhang F, Ao Z and Nie Z, 2019. Temperature-dependent thermal decomposition pathway of organic–inorganic halide perovskite materials. Chem. Mater. **31**: 8515–8522.
19. Juarez-Perez E J, Hawash Z, Raga S R, Ono L K and Qi Y, 2016. Thermal degradation of $CH_3NH_3PbI_3$ perovskite into NH_3 and CH_3I gases observed by coupled thermogravimetry–mass spectrometry analysis. Energy Environ. Sci. **9**: 3406–3410.
20. Su P, Liu Y, Zhang J, Chen C, Yang B, Zhang C and Zhao X, 2020. Pb-based perovskite solar cells and the underlying pollution behind clean energy: dynamic leaching of toxic substances from discarded perovskite solar cells. J. Phys. Chem. Lett. **11**: 2812–2817.
21. Babayigit A, Thanh D D, Ethirajan A, Manca J, Muller M, Boyen H-G and Conings B, 2016. Assessing the toxicity of Pb-and Sn-based perovskite solar cells in model organism Danio rerio. Sci. Rep. **6**: 18721.
22. Eckhardt K, Bon V, Getzschmann J, Grothe J, Wisser F M and Kaskel S, 2016. Crystallographic insights into $(CH_3NH_3)_3(Bi_2I_9)$: a new lead-free hybrid organic–inorganic material as a potential absorber for photovoltaics. Chem. Commun. **52**: 3058–3060.
23. Kopacic I, Friesenbichler B, Hoefler F S, Kunert B, Plank H, Rath T and Trimmel G, 2018. Enhanced performance of germanium halide perovskite solar cells through compositional engineering. ACS Appl. Energy Mater. **1**: 343–347.
24. Lye Y-E, Chan K-Y and Ng Z-N, 2023. A review on the progress, challenges, and performances of tin-based perovskite solar cells. Nanomater. **13**: 585.
25. Boopathi K M, Karuppuswamy P, Singh A, Hanmandlu C, Lin L, Abbas S A, Chang C C, Wang P C, Li G and Chu C W, 2017. Solution-processable antimony-based light-absorbing materials beyond lead halide perovskites. J. Mater. Chem. A. **5**: 20843–20850.
26. Cao J, Tai Q, You P, Tang G, Wang T, Wang N and Yan F, 2019. Enhanced performance of tin-based perovskite solar cells induced by an ammonium hypophosphite additive. J. Mater. Chem. A. **7**: 26580–26585.
27. Thakur S, Borah S M and Adhikary N C, 2018. A DFT study of structural, electronic and optical properties of heteroatom doped monolayer graphene. Optik. **168**: 228–236.

28. Yu Z-L, Ma Q-R, Liu B, Zhao Y-Q, Wang L-Z, Zhou H and Cai M-Q, 2017. Oriented tuning the photovoltaic properties of γ-$RbGeX_3$ by strain-induced electron effective mass mutation. J. Phys. D: Appl. Phys. **50**: 465101.
29. Erdinc F, Dogan E K and Akkus H, 2019. Investigation of structural, electronic, optic and elastic properties of perovskite $RbGeCl_3$ crystal: a first principles study. Gazi Univ. J. Sci. **32**: 1008–1019.
30. Jong U-G, Yu C-J, Kye Y-H, Choe Y-G, Hao W and Li S, 2019. First-principles study on structural, electronic, and optical properties of inorganic Ge-based halide perovskites. Inorg. Chem. **58**: 4134–4140.
31. Houari M, Bouadjemi B, Matougui M, Haid S, Lantri T, Aziz Z, Bentata S and Bouhafs B, 2019. Optoelectronic properties of germanium iodide perovskites $AGeI_3$ (A= K, Rb and Cs): first principles investigations. Opt. Quant. Electron. **51**: 1–14.
32. Huang L-Y and Lambrecht W R, 2016. Electronic band structure trends of perovskite halides: beyond Pb and Sn to Ge and Si. Phys. Rev. B. **93**: 195211.
33. Liu G, Kong L, Gong G, Yang W, Mao H-K, Hu Q, Liu Z, Schaller D R, Zhang D and Xu T, 2017. Pressure–induced bandgap optimization in lead-based perovskites with prolonged carrier lifetime and ambient retainability. Adv. Funct. Mater. **27**: 1604208.
34. Kong L, Liu G, Gong J and Mao H-K, 2016. Simultaneous band-gap narrowing and carrier-lifetime prolongation of organic–inorganic trihalide perovskites. Proc. Nat. Acad. Sci. **113**: 8910–8915.
35. Postorino P and Malavasi L, 2017. Pressure-induced effects in organic–inorganic hybrid perovskites. J. Phys. Chem. Lett. **8**: 2613–2622.
36. Szafrański M and Katrusiak A, 2017. Photovoltaic hybrid perovskites under pressure. J. Phys. Chem. Lett. **8**: 2496–2506.
37. Wang P, Guan J, Galeschuk D T K, Yao Y, He C F, Jiang S, Zhang S, Liu Y, Jin M, Jin C and Song Y, 2017. Pressure-induced polymorphic, optical, and electronic transitions of formamidinium lead iodide perovskite. J. Phys. Chem. Lett. **8**: 2119–2125.
38. Lü X, Wang Y, Stoumpos C C, Hu Q, Guo X, Chen H, Yang L, Smith S J, Yang W, Zhao Y, Xu H, Kanatzidis G M and Jia Q, 2016. Enhanced structural stability and photo responsiveness of $CH_3NH_3SnI_3$ perovskite via pressure-induced amorphization and recrystallization. Adv. Mater. **28**: 8663–8668.
39. Mitro S K, Saiduzzaman M, Asif I T and Hossain M K, 2022. Band gap engineering to stimulate the optoelectronic performance of lead-free halide perovskites $RbGeX_3$ (X= Cl, Br) under pressure. J. Mater. Sci.: Mater. Electron. **33**: 13860–13875.
40. Islam J and Hossain A A, 2020. Semiconducting to metallic transition with outstanding optoelectronic properties of $CsSnCl_3$ perovskite under pressure. Sci. Rep. **10**: 14391.
41. Ali M A, Ullah R, Murad S, Dar S A, Khan A, Murtaza G and Laref A, 2020. Insight into pressure tunable structural, electronic and optical properties of via DFT calculations. Eur. Phys. J. Plus. **135**: 309.
42. Gonze X, Jollet F, Araujo F A, Adams D, Amadon B, Applencourt T, Audouze C, Beuken J-M, Bieder J, Bokhanchuk A, Bousque E T, Bruneval F, Caliste D, Cot M E, Dahm F, Pieve F D, Delaveau M, Gennaro M D, Dorado B, Espejo C, Geneste G, Genovese L, Gerossier A, Giantomassi M, Gillet Y, Hamann D R, He L, Jomard G, Janssen J L, Roux S L, Levitt A, Lherbier A, Liu F, Lukacevi I C, Martin A, Martins C, Oliveira M J T, Ponce S, Pouillon Y, Rangel T, Rignanese G-M, Romero A H, Rousseau B, Rubel O, Shukri A A, Stankovski M,

Torrent M, Van Setten M J, Van Troeye B, Verstraete M J, Waroquiers D, Wiktor J, Xu B, Zhou A and Zwanziger J W, 2016. Recent developments in the ABINIT software package. Comp. Phys. Commun. **205**: 106–131.

43. Perdew J P, Burke K and Ernzerhof M, 1996. Generalized gradient approximation made simple. Phys. Rev. Lett. **77**: 3865–3868.
44. Goedecker S, Teter M and Hutter J, 1996. Separable dual-space Gaussian pseudopotentials. Phys. Rev. B. **54**: 1703–1710.
45. Krack M, 2005. Pseudopotentials for H to Kr optimized for gradient-corrected exchange-correlation functionals. Theor. Chem. Accounts. **114**: 145–152.
46. Monkhorst H J and Pack J D, 1976. Special points for Brillouin-zone integrations. Phys. Rev. B. **13**: 5188–5192.
47. Sharma S and Ambrosch-Draxl C, 2004. Second-harmonic optical response from first principles. Physica Scripta. **2004**: 128–134.
48. Lucarini V, Saarinen J J, Peiponen K-E and Vartiainen E M. Kramers–Kronig Relations in Optical Materials Research. Vol. 110. Springer Science & Business Media, 2005.
49. Kornilovich A and Loseva N, Computer simulation of physical processes in Josephson junction. In: 4th International Conference on Actual Problems of Electronic Instrument Engineering Proceedings. APEIE-98 (Cat. No. 98EX179). 1998. IEEE.
50. Birch F, 1947. Finite elastic strain of cubic crystals. Phys. Rev. **71**: 809–824.
51. Houari M, Bouadjemi B, Haid S, Matougui M, Lantri T, Aziz Z, Bentata S and Bouhafs B, 2020. Semiconductor behavior of halide perovskites $AGeX_3$ (A= K, Rb and Cs; X= F, Cl and Br): first-principles calculations. Ind. J. Phys. **94**: 455–467.
52. Parrey K A, Farooq T, Khandy S A, Farooq U and Gupta A, 2019. First principle studies on structure, magneto-electronic and elastic properties of photovoltaic semiconductor halide ($RbGeI_3$) and ferromagnetic half metal oxide ($RbDyO_3$). Comp. Condens. Matter. **19**: e00381–e00388.
53. Zhu Y Z, Chen G D, Ye H, Walsh A, Moon C Y and Wei Su-H, 2008. Electronic structure and phase stability of MgO, ZnO, CdO, and related ternary alloys. Phys. Rev. B. **77**: 245209.
54. Li Y-H, Walsh A, Chen S, Yin W-J, Yang J-H, Li J, Da Silva J L F, Gong X G and Wei S-H, 2009. Revised ab initio natural band offsets of all group IV, II–VI, and III–V semiconductors. Appl. Phys. Lett. **94**: 212109.
55. Abdulla H T and Sami S A, 2023. First-principles study of structural, electronic, elastic and optical properties of alkali lead iodides $MPbI_3$ (M= Li, Na, K). Ukr. J. Phys. Opt. **24**: 1–21.

Bewar M. Ahmad, Nawzad A. Abdulkareem and Sarkawt A. Sami. 2023. Tuning bandgap and optical properties of Pb-free perovskites $RbGeX_3$ (X = Cl, Br and I) under pressure: a DFT study. Ukr.J.Phys.Opt. 24: 200 – 221. doi: 10.3116/16091833/24/3/200/2023

Анотація. *Досліджено структурні, електронні та оптичні властивості неорганічних безсвинцевих галоїдних перовскитів $RbGeX_3$ (X = Cl, Br та I) під гідростатичним тиском, які можуть посприяти розробці нових оптоелектронних пристроїв і технологій створення сонячних елементів. Застосовано першопринципні розрахунки на основі загального градієнтного наближення в рамках теорії функціоналу густини. Показано, що ширина забороненої зони вивчених перовскитів зменшується зі зростанням тиску. За даного тиску заборонена зона звужується при переході від атома галогену Cl до I. Визначено щільність електронних станів і показано, що рівні енергії поблизу рівня Фермі суттєво змінюються*

під тиском. Оптичні властивості розраховано за допомогою теорії збурень функціоналу густини та співвідношення Крамерса–Кроніга. Для різних тисків розраховано такі оптичні параметри як дійсна та уявна частини діелектричної проникності, показник заломлення та коефіцієнт поглинання.

***Ключові слова**: електронна зонна структура, оптичні властивості, гідростатичний тиск, ширина забороненої зони, густина станів, теорія функціоналу густини, загальне градієнтне наближення.*